BRADLEY G. BOONE, SCOTT A. GEARHART, OODAYE B. SHUKLA, and DAVID H. TERRY

OPTICAL PROCESSING FOR RADAR SIGNAL ANALYSIS

Radar system developers have shown renewed interest in optical signal processing because of progress in electro-optical component technology. This technology promises to advance to the point where certain key processing functions, such as correlation and spectral analysis, can be performed with better speed and efficiency than those of current digital systems. APL has identified appropriate systems applications, is conducting detailed evaluations of component performance, and has conceived novel architectures of radar image processors that obviate some current component limitations.

INTRODUCTION

Recent work at APL has addressed the feasibility of using optical signal-processing technology in radar signal analysis. Optical signal-processing architectures are being evaluated in terms of their performance as limited by commercial components. Assessments have considered synthetic aperture radar (SAR) image generation, feature extraction (especially from range-only profiles derived from real-beam radar), and angle-of-arrival estimation of passively detected radar emissions.

The objective of the APL work has been not only to survey and assess the potential for inserting optical processors in existing RF systems, but to test and evaluate optical signal-processing components in simple precursor architectures. As a result of APL's work, a clear understanding of the limitations of optical processing has emerged. Because of the limitations of component performance, some novel architectures that obviate these limitations are being investigated.

The following sections describe the basics of optical signal processing in a historical, synoptic, and tutorial manner. Important Navy applications, such as surveillance and terminal engagement of surface contacts, provide the context for APL's interest in SAR applications and motivate a concentration on spectral analysis, which is common in many RF subsystems. This article describes recent analytical and experimental investigations that focus on the aforementioned applications. Future work calls for investigating component limitations on processor performance as well as novel architectures of radar image processors.

THEORETICAL BACKGROUND

One of the fundamental properties of light propagation through apertures is diffraction. Sommerfeld[1] defined diffraction as "any deviation of light rays from rectilinear paths that cannot be interpreted as reflection or refraction." A much better picture of the effects of diffraction in practice (for multiple apertures) based on the wave nature of light emerges from considering the constructive and destructive interference that occurs in Young's double-slit experiment.

For the diffraction of plane waves passing through a single aperture, the light pattern created on a viewing screen behind the aperture is substantially different in two regions. At close range, compared with the size of the aperture, the region is called the Fresnel region; at long range, it is called the Fraunhofer region. The Fresnel and Fraunhofer diffraction patterns created by a plane wave passing through a rectangular aperture are shown in Fig. 1. As can be seen, the Fraunhofer pattern of a rectangular aperture is a $(\sin f)/f$ (widely known as sinc f) function along one axis (either x or y), where f is a spatial frequency variable having dimensions of inverse length (that is, cycles per millimeter, analogous to cycles per second).

The far-field diffraction pattern $A(f)$ is, in general, the Fourier transform of the aperture transmittance function $a(x)$ and is given by

$$A(f) = \int_{-\infty}^{\infty} a(x) \exp(-j2\pi fx)\, dx \ , \qquad (1)$$

where x is the spatial distance. The rectangular aperture $a(x,y)$ is expressed by

$$a(x,y) = \mathrm{rect}(x/x_0)\ \mathrm{rect}(y/y_0) \ , \qquad (2)$$

where

$$\mathrm{rect}(x/x_0) = \begin{cases} 1 & |x| \le x_0 \\ 0 & |x| > x_0 \ , \end{cases}$$

and

$$\mathrm{rect}(y/y_0) = \begin{cases} 1 & |y| \le y_0 \\ 0 & |y| > y_0 \ . \end{cases}$$

The Fourier transform $A(f_x, f_y)$ of the rectangular aperture $a(x,y)$ is given by

$$A(f_x, f_y) =$$

$$x_0\ y_0\ [\sin(\pi fx_0)/(\pi fx_0)]\ [\sin(\pi fy_0)/(\pi fy_0)] \ , \qquad (3)$$

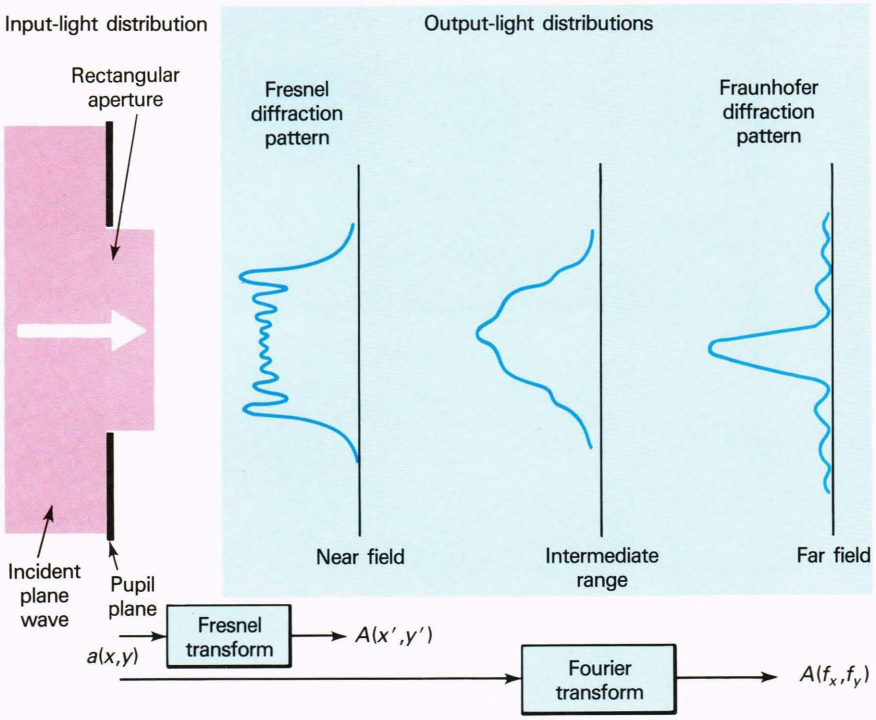

Figure 1—Transition from Fresnel to Fraunhofer diffraction for a rectangular aperture.

where f_x and f_y are the spatial frequencies along the x and y axes, respectively, and x_0 and y_0 are the corresponding dimensions of the rectangular aperture. For distances closer to the aperture, the Fraunhofer pattern changes to the Fresnel pattern. In the limit of zero distance from the aperture, the Fresnel pattern becomes a geometrical shadow of the aperture, as shown in Fig. 1.

The Fresnel transform describes the relationship between the input-light and output-light amplitude distributions shown in Fig. 1 and is given by

$$A(x',y',z) = \frac{\exp(jkz)}{j\lambda z} \times \int_{-\infty}^{\infty}\int_{-\infty}^{\infty} a(x,y)\, \exp\{j\,(k/2z)\,[(x-x')^2 + (y-y')^2]\}\, dx'\, dy' , \quad (4)$$

where $A(x',y',z)$ is the output plane-light amplitude distribution, $a(x,y)$ is the input (or pupil) plane-light amplitude distribution, x and y are the input spatial distance variables, x' and y' are the output spatial distance variables, z is the distance along the optical path, λ is the wavelength, and k is the spatial wave number ($k = 2\pi/\lambda$). The integral of Eq. 4 takes the form of a convolution (or correlation). If the input-light distribution is a plane wave and the pupil-plane shape is a rectangle, then Eq. 4 reduces to the well-known Fresnel integral, which was commonly evaluated nomographically by using the cornu spiral in the days before modern digital computation.

Equations 1 and 4 lead to a view of optical systems that is familar to electrical engineers. The principle of linear superposition, as well as the restriction of using paraxial rays in light propagation through optical systems, leads to the linear space-invariant systems approach. Thus, optical components are treated as linear system components, with their appropriate input and output waveforms and transfer functions. For Fraunhofer diffraction, this view is illustrated in the lower part of Fig. 1. In this case, an image can be decomposed into its constituent spatial frequency components, just as a temporal electrical waveform can be decomposed into its constituent temporal frequency components. The linear systems approach to optics is often called Fourier optics.

An important result of Fourier optics is that a lens inserted at the pupil plane of Fig. 1 adds a quadratic phase variation across the aperture to the incident plane wave. This variation yields a Fraunhofer diffraction pattern, that is, a Fourier transform at close range rather than at long range, as expected in ordinary Fraunhofer diffraction. Under these circumstances, if a transparency is placed one focal distance in front of the lens and illuminated with a coherent plane wave, its exact Fourier transform will be produced one focal distance behind the lens, as shown in Fig. 2 (similar to the simple aperture described in Fig. 1). All spatial distances in the Fourier output plane are then related to the spatial frequency f in Eq. 4 through the expression x'(or y') $= \lambda F f$, where F is the lens focal length. If the object is not at the focal distance, an exact Fourier transform will not be obtained because of extra phase factors, but an exact power spectrum can be obtained.

PREVIOUS INVESTIGATIONS

The roots of optical signal processing are the early work of Abbe[2] on the spatial filtering of microscope images, as well as the invention of the phase-contrast

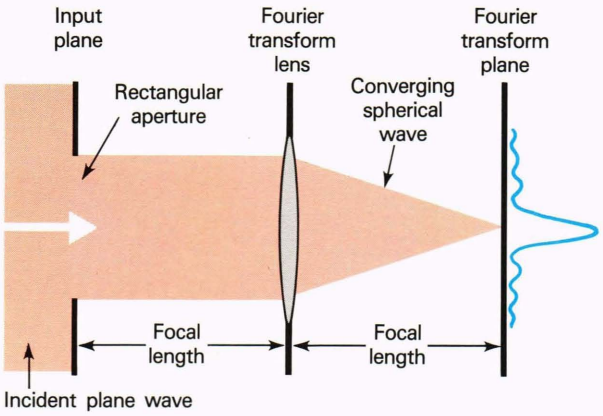

Figure 2—Simplified optical Fourier transform architecture.

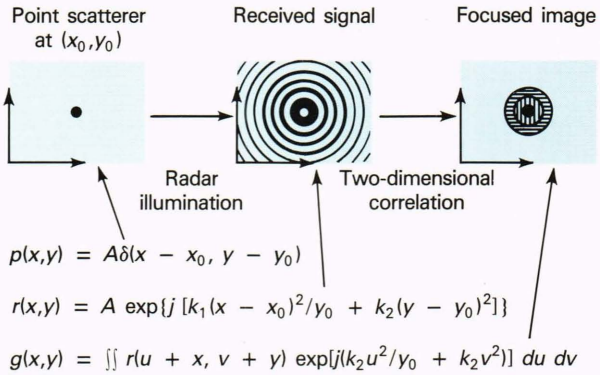

Figure 3—SAR imaging process. The basic mathematical operation can be viewed as either a Fourier transform, a correlation, or a Fresnel transform.

microscope by Zernike.[3] In the early 1950s, several branches of the field evolved,[4] including work directed toward SAR,[5] pattern recognition,[6] matched filtering,[7] spectral analysis,[8] and optical computing.[9] Optical processing is a multidisciplinary field involving hybrid technology and substantial pragmatic rather than deep theoretical underpinnings. In the United States, various technology thrusts stimulated the development of certain key tools: laser diodes (for fiber-optic communications), charge-coupled device or charge-injection device cameras (for industrial inspection, optical astronomy, etc.), and acousto-optic spatial light modulators (for optical beam scanning). In the Soviet Union, two-dimensional spatial light modulators have been the subject of productive research and development.[10] In recent years, investigators have focused on algorithms and architectures for the application of optical processing to feature extraction (Casasent[11]), temporal signal processing (Spezio and Lee[12]), and acousto-optic SAR processing (Haney and Psaltis[13]). These researchers have had the greatest influence on recent work at APL.

The association of optical processing with SAR image generation dates back to the work of Cutrona et al.[5] at the University of Michigan. The most relevant current work on SAR image generation is that of Haney and Psaltis.[13] Their work has renewed serious interest in optical SAR processing because their architectures use the component technologies mentioned earlier (acousto-optic cells, charge-coupled devices, and laser diodes) to achieve real-time SAR image generation.

In SAR image generation, as shown in Fig. 3, the basic mathematical operation can be viewed as either a Fourier transform, a correlation (or matched filter), or a Fresnel transform. These operations are all equivalent in SAR processing. Close examination of the equations in Fig. 3 confirms this assertion. Optical signal-processing techniques are naturally suited to SAR image formation because the coherent detection of radar echoes received from the object field in SAR is analogous to the interferometric detection of the Fresnel diffraction pattern of an object illuminated with coherent light. Therefore, the synthesis of the image of a single-point scatterer is equivalent to the optical reconstruction of a Fresnel hologram of a single point.

In SAR imaging, Haney and Psaltis[13] take advantage of the separability of the slant-range (x) and cross-range (y, azimuth) processing steps. In their architecture, two Bragg cells are used: one that processes in slant range and one that processes in azimuth. This processor has been demonstrated by using synthetic signals that represent single[13] and multiple[14] point targets. The first (slant-range processing) stage of this architecture has been the focus of acousto-optic work at APL.

NAVY APPLICATIONS

The U.S. Navy is often interested in remote sensing using radar sensors, especially high-resolution sensors for imaging and recognition of man-made objects. In a military mission, this requirement usually translates into surveillance or terminal guidance. In particular, the Navy is continually interested in exploring the use of radar sensors for ocean surveillance, land-scene mapping for strike warfare, and high-resolution sensing of radar surface contacts before or during antiship missile engagement.

In ocean surveillance, which is needed for the employment of antiship missiles, large areas must be surveyed or mapped at modest spatial resolution to determine the locations or possibly the overall sizes of the desired targets. Subsequently, higher resolution images of specific contacts must be created to classify potential high-value targets for terminal engagement. Sensors such as SAR are prime candidates for these tasks. Compact SAR sensors that can generate imagery in real time while on board satellite or airborne platforms and missiles are desired.

Other sensors may be used to enable Navy platforms (especially aircraft and antiship missiles) to detect, locate, and possibly classify surface contacts. It has been shown experimentally that conventional real-beam radar can be used to derive one-dimensional functions of target radar cross sections (range profiles), which can be used to classify targets. Electronic support measures can be used to passively detect, locate, and classify potential threats by their characteristic radar emissions. All

of these sensors, including SAR, use a common preprocessing function, namely, spectral analysis. Spectral analysis is one way to look at the fundamental mathematical operation involved in beam forming, which occurs in SAR, electronic support measures, and feature extraction from radar range profiles. This mathematical operation is actually the Fourier transform. In some instances, especially SAR image formation and the matching of images, correlation is another way of looking at the required processing.

Optical processing, as already discussed, performs correlation and spectral analysis very well. Some optical-processing architectures are natural analogs to the sensing operation itself, as is the case for SAR. The problem arises when these architectures must be implemented with current technology. Constraints on the performance of individual components limit the intended signal-processing functions performed by the architectures.

APL INVESTIGATIONS

Over the past few years, an APL effort has focused on the application of optical signal processing to radar systems, particularly SAR image generation. This effort has also involved a survey and assessment of optical-processing architectures in various applications of potential interest to the Navy, especially spectral analysis of radar signals. Continuing work has addressed the testing and evaluation of optical signal-processing components, most notably laser diodes, acousto-optic modulators, Bragg cells, liquid-crystal televisions, and solid-state cameras. Both analytical and experimental efforts have been conducted. The concern for the limitations of component technology is motivated by the desire to use off-the-shelf (commercial) technology because it is cheaper and more accessible. Even state-of-the-art components will limit the ability of optical signal processing to reach its full theoretical potential.

The simple Fourier transform architecture shown in Fig. 2 provides the basis for the ensuing discussion of our laboratory evaluations of optical-processing components and their effect on the spectral analysis of video signals. In place of a static transparency in the object plane, a spatial light modulator is used. It is generally illuminated with either a continuous gas laser or a pulsed solid-state laser. The output light is detected by either a one- or two-dimensional solid-state detector array. Variants of this simple architecture, according to the types of components used, will be presented later.

Optical-Processing Components

One of the earliest investigations conducted at APL involved measuring the coherence properties of laser diodes. Coherent light sources for the illumination of spatial light modulators are especially important in interferometric architectures. In these architectures, two light beams interfere to create a light pattern that must be detected by a square-law detector array. Laser diodes are preferred because of their small size, high modulation bandwidths, and efficiency. Laser diodes that emit highly monochromatic light, however, are limited in their output power. This means that if you need high power in an optical processor, you must sacrifice coherence length; similarly, if you need coherence length, you must sacrifice optical power. The laser diodes used for this effort were gallium aluminum arsenide injection laser diodes (made by RCA), and they emitted just beyond the visible region, between 810 and 830 nm. Typical peak pulse powers were several watts, pulse lengths were 10 to 100 ns, and pulse repetition frequencies were 1 to 26 kHz.

Tests have shown that single-mode, index-guided diode lasers have sufficient coherence but typical peak output powers of only 30 mW.[15] Because multimode, gain-guided laser diodes (such as the RCA type) have significantly higher output power, and because we initially thought that their coherence would not deter us from achieving useful results in power spectral analysis, we proceeded to use them. The coherence properties were nevertheless of concern, especially when the diodes were used in conjunction with acousto-optic Bragg cells, so we decided to measure coherence.

In measuring coherence, several parameters must be considered: coherence length during the pulse (intrapulse coherence), coherence (or frequency stability) from pulse to pulse, lateral spatial coherence, and time delay before coherence occurs during a pulse. Longer delays between the time that the trigger starts a pulse to the time that coherence is achieved lead to larger amounts of noncoherent stray light. This situation contributes to reduced dynamic range. Intrapulse coherence must be sufficiently long so that a beam traversing the Bragg cell will remain coherent from one side of the cell to the other, as required by interferometric architectures. Frequency stability (from pulse to pulse) is required in time-integrating as well as interferometric architectures. Finally, lateral spatial coherence is required to enable spatially extended interferometric (image) processing.

The test apparatus that measured laser diode coherence, shown in Fig. 4, consists principally of a Michelson interferometer. Laser beams along two different paths interfere at the detector when the coherence length is greater than the optical path difference between the two beams. The optical path difference when no amplitude interference is observed equals the coherence length. The resulting variation of amplitude is the fringe pattern, whose modulation depth is called fringe contrast.

To observe interference, the optical path difference is set to zero. One mirror is dithered, forcing the beams to interfere from pulse to pulse over many cycles that span from constructive to destructive interference. A fast silicon photodiode is used for detection, and the total temporal interference envelope is displayed on an oscilloscope, as shown in Fig. 5a. This display is the result of overlaying many detected pulses. The depth of the envelope is a measure of fringe contrast. As the optical path difference is varied from zero, fringe contrast decreases (Fig. 5b), until finally no constructive interference occurs (Fig. 5c).

Figure 6 is a plot of fringe contrast versus optical path difference for several laser diode maximum current settings and pulse repetition frequencies. Lower current im-

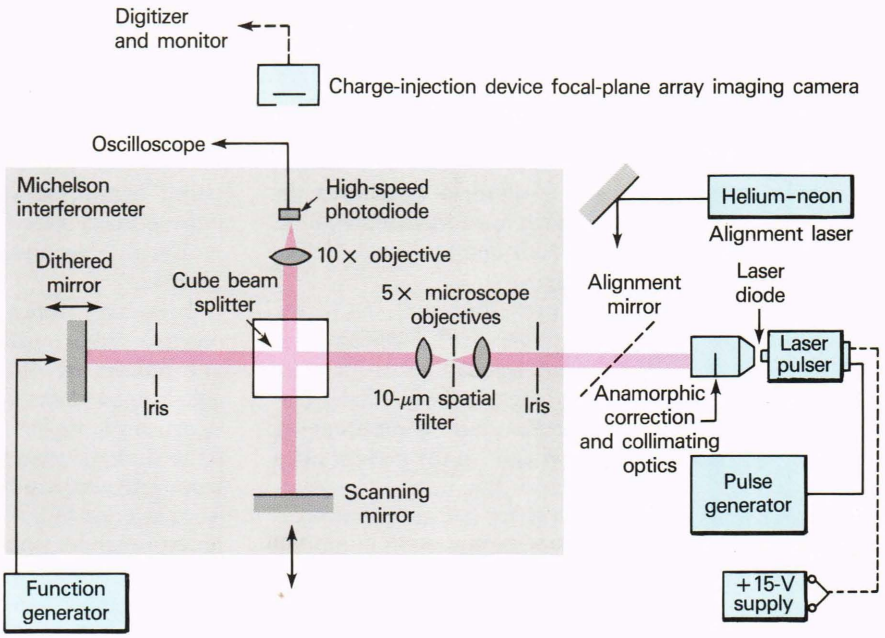

Figure 4—Test setup for laser diode coherence measurements.

plies fewer laser modes, which imply better coherence. No differences were observed for different pulse repetition frequencies. Intrapulse coherence length was determined to be about 0.3 mm, which is consistent with theoretical expectations, given the spectral bandwidth provided by the manufacturer. Such a short coherence length is unacceptable for interferometric processing and is considerably less than the typical Bragg-cell depth, which is about 5 mm.

To examine spatial coherence, a spatial filter is placed in front of the beam splitter to remove potential spatial coherence degradations of the laser beam that could deter the measurements. A charge-injection device is placed in lieu of the single photodiode, and the output beams are misaligned, first in the horizontal and then in the vertical plane. Since the camera has a 60-Hz field rate and the laser diode has an 8-kHz pulse repetition frequency, the number of pulses integrated on the charge-injection device is 133. If the laser beam frequency is stable from pulse to pulse, the fringe contrast will be high. Figures 7a and 7b indicate some degree of pulse-to-pulse stability.

To observe the effect of spatial phase distortion across the laser beam, the spatial filter was removed and the beams were displaced in angle both horizontally and vertically, as in Figs. 7a and 7b. Good fringe visibility versus horizontal displacement was observed, as shown in Fig. 7c, which implies good spatial coherence in the horizontal direction. Poor fringe visibility for vertical displacement was observed, as shown in Fig. 7d, which implies poor spatial coherence in the vertical direction. The vertical direction is parallel to the laser junction. The causes of these results may be multiple modes exiting in the vertical plane at different angles or distortion due to a poor-quality laser diode case window. The outcome of these measurements is that these particular high-powered pulsed laser diodes are unsuitable for interferometric optical processing.

The time delay before coherence occurs is measured from the leading edge of the pulses shown in Figs. 5a to 5c to the point along the waveform where significant interference is observed. Figures 5a to 5c indicate that the laser becomes coherent in a very short time from the pulse leading edge. A detailed measurement was not necessary, however, because the poor temporal coherence already precluded this laser from additional consideration.

In a typical optical-processing architecture, the laser diode is followed by a spatial filter, beam collimator, and expander to produce an approximately uniform plane wave with sufficient beam width to flood the aperture of the spatial light modulator. This configuration is shown later (Fig. 12). To expedite initial testing with coherent and visible light, a helium–neon continuous-wave gas laser may also be used. For pulsed operation, an acousto-optic modulator that chops the input laser beam would be necessary.

Following the laser source, the spatial light modulator is used in the pupil plane to modulate the incident light. Two types of spatial light modulators have been assessed: acousto-optic Bragg cells and liquid-crystal televisions (LCTVs). Bragg cells were initially chosen because they have higher performance and are suitable for a greater variety of tasks, including interferometric processing of SAR images. LCTVs are two-dimensional spatial light modulators and are much cheaper than Bragg cells ($100 each versus $12,000 each). Both types of devices are electrically addressed, so they can be conveniently interfaced with traditional electrical systems, particularly raster video modulation equipment. This situation makes laboratory testing and evaluation more convenient for feasibility studies.

The Bragg cell consists of a tellurium dioxide crystal with a piezoelectric transducer attached to one end. Electrical modulation injected at the transducer sets up a slow-shear traveling acoustic wave in the crystal medi-

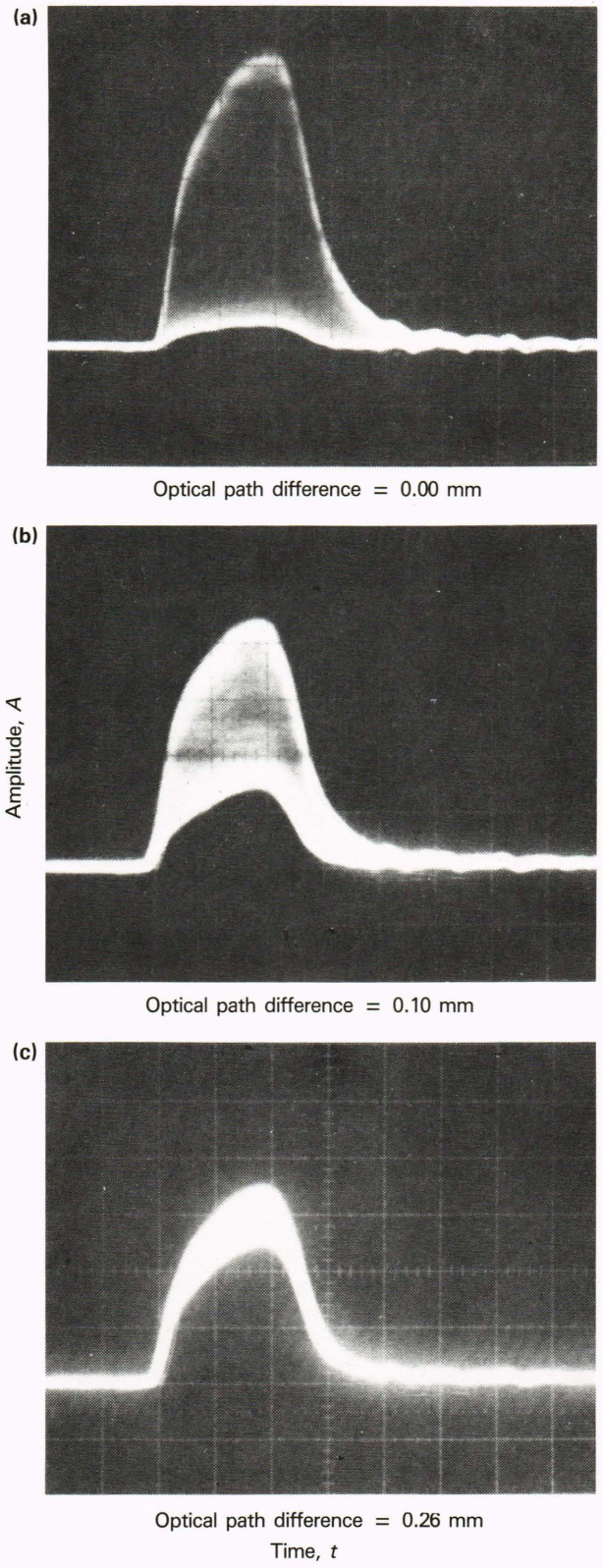

Figure 5—Fringe contrast (average pulse envelope) versus optical path difference. The test conditions were the following: maximum laser current, pulse repetition frequency of 8.3 kHz, pulse width of 14 ns, no spatial filtering, and fixed mirror dithered.

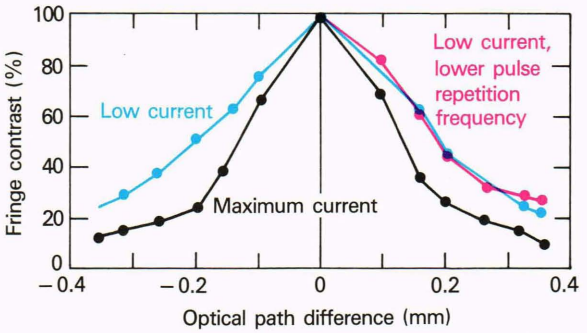

Figure 6—Results of intrapulse coherence tests showing fringe contrast versus optical path difference.

um. This elastic disturbance pattern matches the amplitude waveform of the temporal modulation of the electrical signal applied at the transducer. Light incident on the Bragg cell is diffracted from the spatial modulation established in the crystal at the so-called Bragg angle, as illustrated in Fig. 8. By flashing the acoustic modulation pattern within the Bragg cell at the instant it fills the aperture with a short burst of laser light, the same pattern is frozen onto the transmitted beam. This is the modulation effect of the Bragg cell.

Diffracted light suffers a deflection in angle. In the small-signal limit, the deflection angle θ outside the cell is proportional to the instantaneous electrical modulation frequency applied at the transducer:

$$\theta \approx \lambda f / v_s \ , \qquad (5)$$

where λ is the optical wavelength, f is the maximum frequency of modulation, and v_s is the velocity of sound in the crystal medium. In practice, the modulating signal must be mixed with a carrier at the Bragg-cell input. Thus, the diffracted-light distribution observed in the detector plane is the double-sideband frequency spectrum of the modulating signal, centered at an angle corresponding to the carrier. For a typical carrier frequency (75 MHz) and tellurium dioxide, this angle is 5.75° at λ = 830 nm. Over the bandwidth of typical television video signals (4 MHz), the deflection angle is about 0.31° (at 830 nm). The 3-dB bandwidth of our Bragg cells, however, is quite large—50 MHz. The large bandwidth coupled with the slow shear of these cells (sound velocities of 620 m/s) and aperture times of 70 μs leads to a time–bandwidth product of 3500. This product is a theoretical measure of the number of resolvable frequencies and in this case is more than adequate. (Aperture time is the transit time across the Bragg cell.) The incident light is also slightly Doppler shifted, but this effect is generally not exploited in optical processing.

The other important performance measure for Bragg cells is their diffraction efficiency, η, which is the ratio of the intensity of the light diffracted into the first-order beam over the intensity of the incident light beam. This parameter is given by

$$\eta = \sin^2[(\pi^2/2\lambda^2)\, M_2\, (l/h)\, P_a]^{1/2} \ , \qquad (6)$$

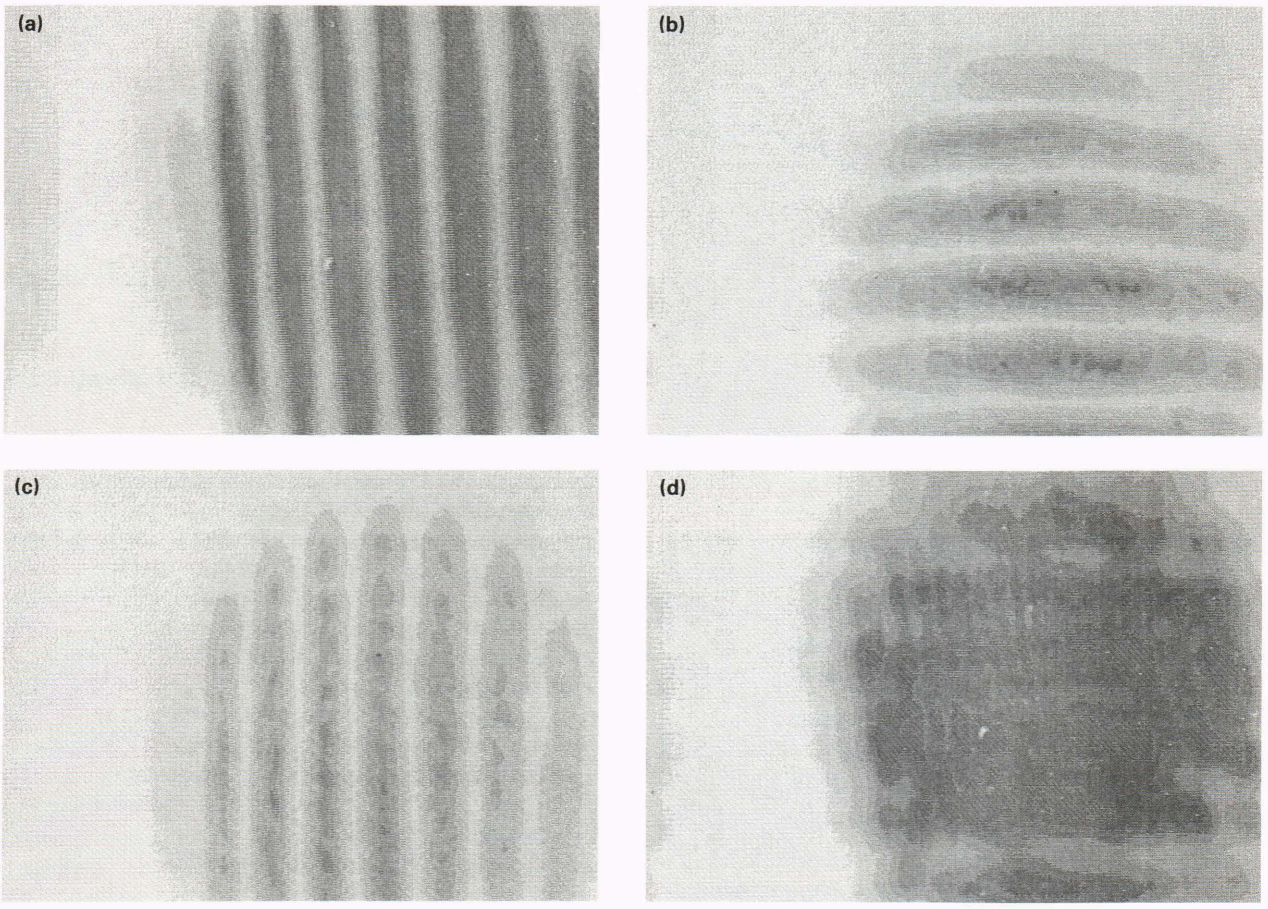

Figure 7—Spatial coherence results with a 10-μm spatial filter for beams misaligned in the (a) horizontal and (b) vertical planes, and spatial coherence results without a spatial filter for beams misaligned in the (c) horizontal and (d) vertical planes.

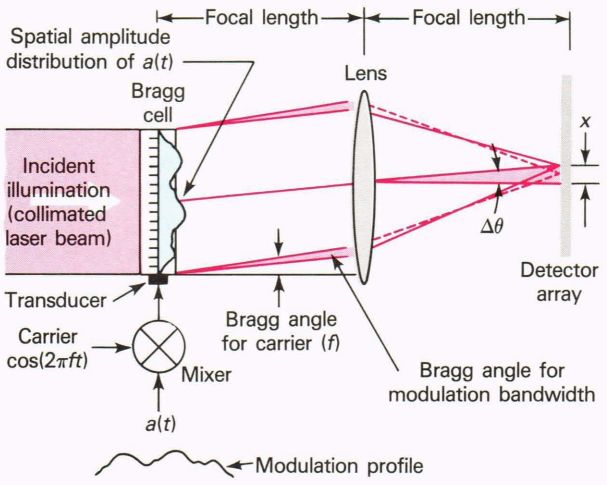

Figure 8—Signal input, acousto-optic diffraction from a typical Bragg cell, and Fourier transform architectural geometry for spectral analysis.

where M_2 is the acousto-optic figure of merit; l and h are the length and height, respectively, of the interaction region between the incident light beam and the acoustic diffraction pattern emanating from the piezo transducer; and P_a is the effective acoustic power ($P_a \approx 0.6\,P_{RF}$, where P_{RF} is the RF modulation power level). The diffraction efficiency η is plotted versus the effective acoustic power P_a in Fig. 9. Up to a certain RF level, the diffraction efficiency is a linear function, although this result is valid only for a single frequency (or tone).

In practical applications, such as spectral analysis of waveforms with multiple tones or the generation of SAR images with multiple-point scatterers, the diffraction efficiency is a more complicated nonlinear function of individual signal strengths, even in the small-signal limit. Hecht[16] showed that for multiple signals, all of equal strength, the diffraction efficiency η_i is given by

$$\eta_i = \eta_1[1 - \tfrac{1}{3}bP_a - \tfrac{2}{3}nbP_a] , \qquad (7)$$

where η_1 is the single-tone diffraction efficiency, b is about 1 W^{-1}, and n is the number of tones. Figure 9 (curves C, D, and E) shows that as the number of tones increases from one to three, the diffraction efficiency decreases substantially in a nonlinear way versus acoustic power. This result indicates that less dynamic range is available for processing large numbers of scatterers (or tones) using Bragg cells. Thus, the theoretical time–

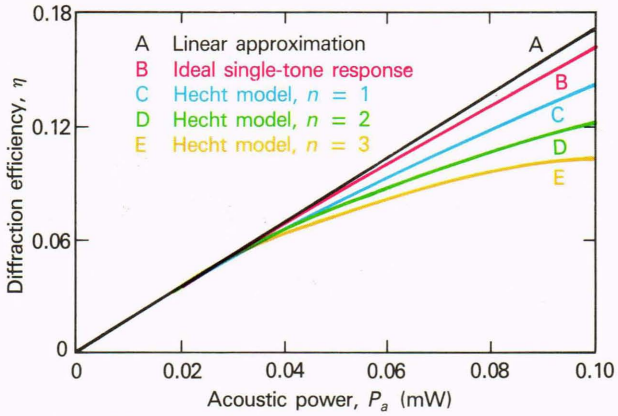

Figure 9—Diffraction efficiency versus acoustic power for single and multiple tones of input acoustic power.

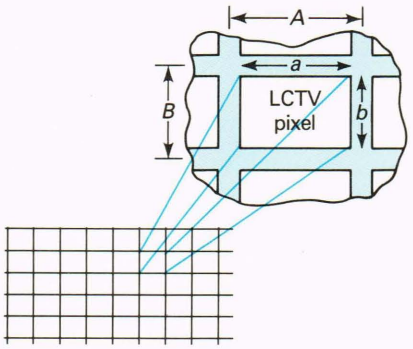

Figure 10—LCTV pixel structure. The inset gives detail on the pixel dimensions.

bandwidth product of 3500 is not usable. For instance, when only two frequencies of equal amplitude are in the Bragg-cell aperture at the same time, dynamic ranges of 50 dB[17] are achievable.

As more tones are added, dynamic range degrades significantly. In addition to dynamic-range loss due to multitone operation, loss from acoustic attenuation across the Bragg-cell aperture also occurs. This loss is about 5 dB for our Bragg cells. It is desirable to keep a narrow bandwidth with respect to the center frequency, which in the case of television video is nominally 5%. For SAR processing, bandwidths of 60 MHz at 75-MHz center frequencies are required. Further, single-pulse durations of 60 μs (requiring time–bandwidth products of 3600) are not uncommon. Thus, manufacturer specifications for off-the-shelf Bragg cells would seem to closely match the requirements for SAR processing. Brute-force spectral analysis for generating SAR images is going to be limited by Bragg-cell performance for the reasons discussed earlier. As will be seen later, less stringent requirements will be demanded by range-profile feature extraction.

We also considered the alternative LCTV spatial light modulator. The LCTV used in our investigations was a commercial device that was modified by removing the diffuser plate, separating the liquid-crystal unit from the television electronics, and using the liquid-crystal unit in a transmissive mode. The pixel structure of the LCTV (Fig. 10) is a 150 by 160 lattice of rectangular pixels, each 340 by 430 μm. The aperture is therefore 54 by 72 mm. Each pixel is electrically addressed by a particular portion of a video waveform using a standard video format. The instantaneous bias created at each pixel site induces a polarization twist on incident light passing through that particular pixel. Polarizing sheets before and after the liquid crystal linearly polarize the light and enable polarization modulation to be converted to amplitude or intensity modulation. Thus, the LCTV spatially modulates an incident wave front or laser beam. The incident light does not have to be coherent, although it should be nearly monochromatic to reduce any undesirable smearing of spectral frequency components in the output plane of a spectrum analyzer.

The two key parameters needed to characterize LCTV performance are spatial resolution and amplitude dynamic range, which is commensurate with the signal-to-noise ratio. The resolution is set by the pixel structure. The number of pixels (150 or 160) gives the effective space–bandwidth product, or number of resolution cells, for signal processing along a given axis. This number is much lower than that for the Bragg cell, but the LCTV is two-dimensional, which results in simpler architectures for accomplishing the same operation. Using coherent light, dynamic range is limited in commercial LCTVs by the low-quality polarizers, which have varying thicknesses and hence varying phase delays from point to point over the LCTV aperture.

Dynamic-range loss is also caused by scattering within the liquid-crystal pixels. These effects contribute to variations in the transmitted-light amplitude that are detected as fixed-pattern noise. Measurements were made of the dynamic range by using both laser and white-light sources in conjunction with an integrating sphere that uniformly illuminated the LCTV, which was subjected to different direct-current levels of video signal. Some of these measurements are summarized in Fig. 11. From these measurements, the dynamic range was estimated to be about 16-to-1 (or 4 bits). Although this value is considerably lower than the dynamic range of a Bragg cell, analysis of the dynamic-range requirements for SAR image generation reveals that 4 bits of dynamic range in the Fourier plane is sufficient to obtain a reasonably good quality digital Fourier transform. This dynamic-range requirement will be discussed later.

The last component in the optical processor is the output-plane detector array, which may be one- or two-dimensional. We used a linear, self-scanned, charge-coupled device array for one-dimensional spectral analysis because it affords higher dynamic range than most two-dimensional arrays. Higher dynamic range is achieved by good low-noise design and thermoelectric cooling, which reduces thermal noise, including dark-current noise. We also used charge-injection device cameras because they are two-dimensional and afford flexible readout schemes, including extended temporal integration of pixel outputs, which achieve higher signal-

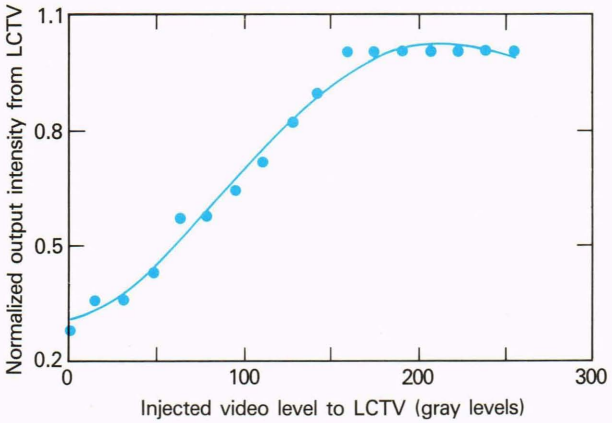

Figure 11—Plot of LCTV output-light intensity versus injected video level for high laser incident power on the LCTV. A polynomial fit to the data is shown.

to-noise ratios. For both types of arrays, fixed-pattern noise caused by nonuniform responsivity is the limiting factor on the dynamic range. For charge-injection device arrays, single-frame signal-to-noise ratios are about 30 dB, whereas single-pixel signal-to-noise ratios of self-scanned arrays approach 47 dB.

Optical-Processing Architectures

Experimental investigations at APL initially concentrated on simple architectures using both Bragg-cell and LCTV spatial light modulators for spectral analysis. Acousto-optic spectral analysis using current (off-the-shelf) components shows the greatest promise of meeting the requirements for large space–bandwidth SAR image processing. LCTV spectral analysis, although of limited performance, is easy to do, inexpensive, and therefore useful for testing concepts before upgrading and tailoring LCTV technology to optical signal-processing requirements.

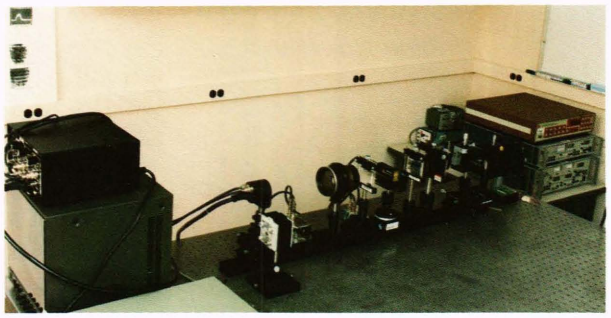

Figure 12—Photograph of the one-dimensional, acousto-optic, Bragg-cell spectrum analyzer.

Figure 12 is a photograph of the laboratory apparatus currently used for one-dimensional spectral analysis. Figure 13 is a detailed diagram of this architecture, which is interesting not only as the first (range-compression) stage of an optical SAR processor, but also from the standpoint of range-profile feature extraction (or spectral analysis).

Tests of the architecture were conducted by using a laser diode pulsed at a pulse repetition frequency of 26 kHz with pulse widths of 14 ns. The charge-injection device array used for detection integrated 433 pulses per output video frame. The RF signal level applied to the Bragg cell was 16 mW for each of the input waveforms shown in Figs. 14a, 14c, and 14e. The corresponding detected double-sided Fourier transforms are depicted in Figs. 14b, 14d, and 14f. The charge-injection device was used in lieu of the linear self-scanned array for Figs. 14a to 14f because the spectra are easier to display. The first side lobes of the discrete sinc functions shown in Figs. 14d and 14f are near the saturation level of the charge-injection device, whereas the furthest visible side lobe is near the noise level. Resolving even higher frequency side lobes would require an increase in system dynamic

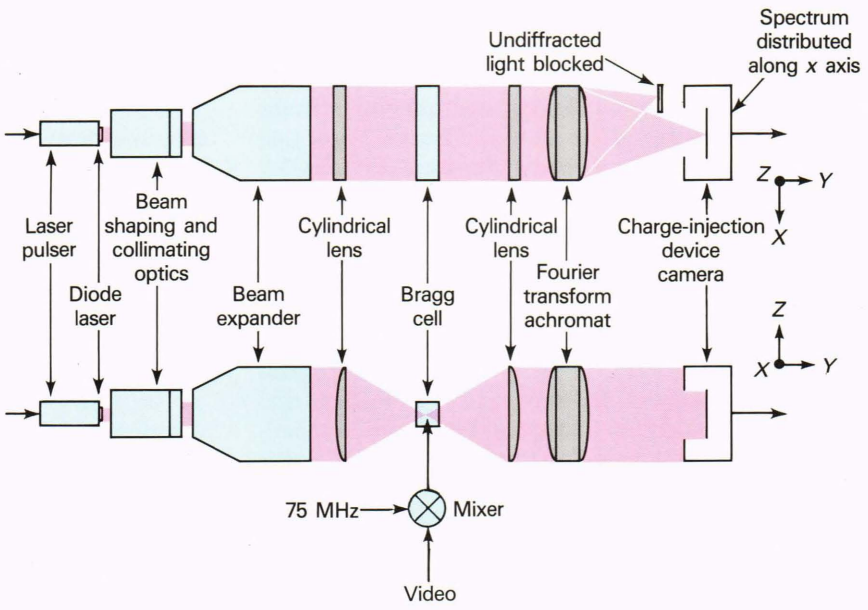

Figure 13—One-dimensional optical-processing architecture for the video spectrum analyzer.

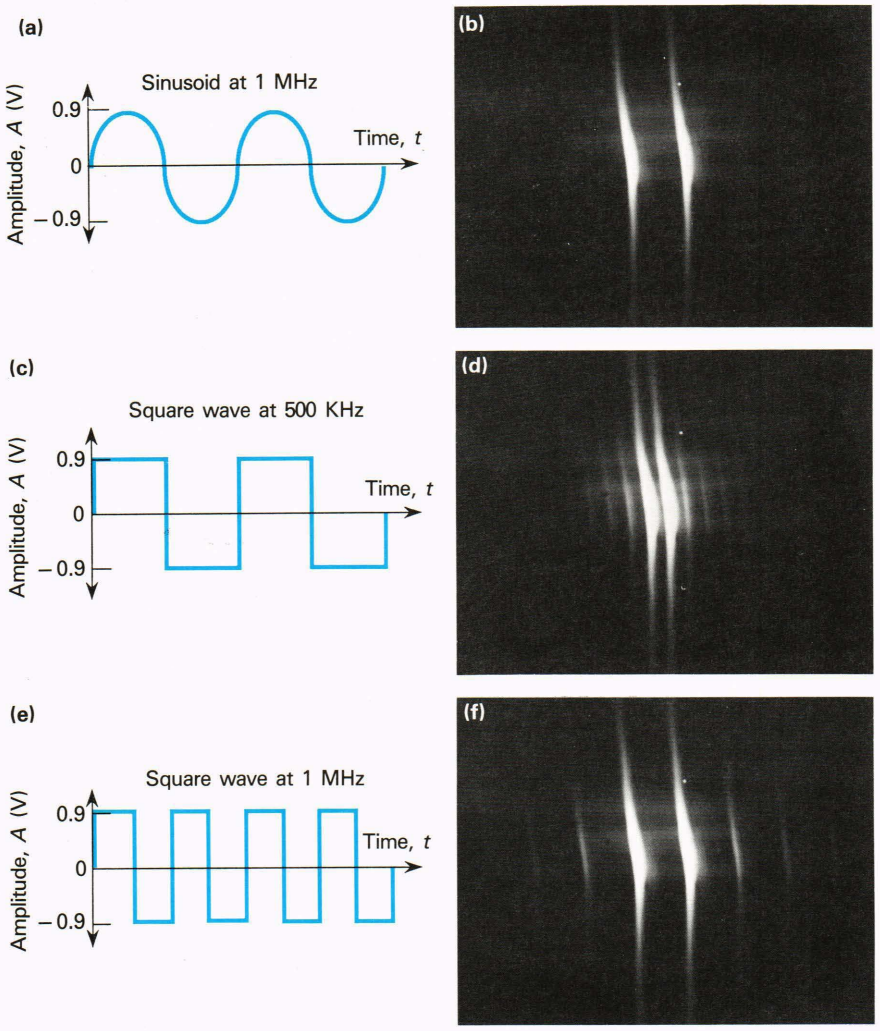

Figure 14—Signal inputs to the Bragg cell: (a) sine wave, (c) square wave, and (e) square wave of higher frequency. The corresponding power spectra are shown in parts b, d, and f, respectively.

range. This increase might be realized by reducing stray background light and by reducing charge-injection device noise through cooling.

An important consideration in this architecture is its overall size and the proper matching of the number of detector pixels to the number of resolvable frequencies in the spectrum. Refer to Fig. 8 for the following discussion. Given that the video bandwidth is 4 MHz, the corresponding deflection angle θ is 0.31°. By using the equation

$$F = x/\Delta\theta \ , \tag{8}$$

where F is the focal length and x is the linear displacement in the detector (or Fourier) plane, a focal length of 1.36 m is consistent with a typical detector array size x_{max} of 0.74 cm. The distance in the Fourier plane corresponding to the spatial frequency of the entire Bragg-cell aperture (which represents the lowest frequency that can be supported by the Bragg cell and the lowest frequency that can therefore be resolved in the spectrum according to Rayleigh's criterion for optical resolving power) is given by

$$\Delta x = \lambda F/l \ , \tag{9}$$

in the small-angle approximation, where λ is the wavelength and l is the Bragg-cell aperture (42 mm). The number of resolvable frequency components is given by $x_{max}/\Delta x = 285$. The minimum resolvable frequency is about 14 kHz, a little lower than the standard television horizontal line rate ($\approx$16 kHz).

Another result of this design exercise is that the overall length of the spectrum analyzer is at least 2.72 m, unless some optical path folding is done. Equation 8 shows that either decreasing the size of the detector array or increasing the deflection angle (or, correspondingly, the modulation bandwidth) will help reduce the overall processor size.

The implication of the multitone analysis discussed earlier is that a modest number of spectral components (on the order of 10 to 100) should be achievable with good dynamic range (approaching 40 dB). This result is compatible with the expected dynamic range of our linear self-scanned array, and it is adequate to support the application of an acousto-optic spectrum analyzer to range-profile feature extraction. In range-profile fea-

ture extraction, the input waveform typically has 10 to 100 independent samples, a modulation bandwidth of 5 to 10 MHz, a pulse repetition frequency of 2 to 5 kHz, a center frequency of 60 MHz, and a single-pulse dynamic range of 25 dB. The actual number of independent frequency resolution cells used from the output-feature vector (power spectrum) is often no more than 10 to 20. These requirements are thought to be within reach of the components and architecture described earlier, but actual analysis and design are the subjects of future investigations.

The other critical system issue is the achievable pixel signal-to-noise ratio or, equivalently, the number of laser pulses required to achieve signal saturation at the linear array detector plane. Consider the following example: The energy E incident on a given detector is given by

$$E = P\,\tau\,T_o\,\eta/2 \approx 8\ \text{nJ}\ , \qquad (10)$$

where P is the laser power, τ is the pulse width, T_o is the optical transmission, and η is the diffraction efficiency. Equation 10 assumes all diffracted light resulting from a single-tone input falls on two detector elements. The peak laser power is 10 W, the pulse width is 10 ns (using our current laser diode modulator), the optical transmission is 0.8, and the diffraction efficiency is 2% per tone. For the Fairchild self-scanned array, the saturation energy E_{sat} is 0.5 μJ. Therefore, the ratio E_{sat}/E is 62, which is the number of pulses required to yield saturation. At a pulse repetition frequency of 2 kHz, the time required to accumulate 62 pulses is only 30 ms, which is a television video frame time. Thus, operating the spectrum analyzer at typical radar pulse repetition frequencies should achieve the signal-to-noise ratio consistent with standard raster modulation rates, a desirable and convenient result for processing data in the laboratory.

Figure 15 is a photograph of an LCTV architecture for spectral analysis of television video images. This architecture is much simpler than the acousto-optic architecture, and it performs the Fourier transform in two dimensions. A detailed diagram of how it should be used is shown in Fig. 16. Basically, the LCTV is injected with a video raster modulation pattern, and a Fourier transform is taken and detected on the output charge-injection device array. A pulsed laser diode can be used to illuminate the LCTV, but in practice we have used a helium–neon continuous-wave laser. For television video, a single-channel input can be used; if a radar video signal were used, both in-phase and quadrature receiver channels could be processed by time-multiplexing them. Time-multiplexing results when interlaced video is used with even and odd fields.

High-frequency artifacts are created in the Fourier plane because of the pixel structure of the LCTV. Artifacts are undesirable and can be blocked out by a spatial filter, as shown in Fig. 16. The only important information in the transform plane lies within a small region (quadrant) bounded by the main lobe at zero spatial frequency and the first side lobes on both axes (f_x and f_y). This region is described by Eq. 12 for the theoretical case of a mathematical model of the LCTV described by

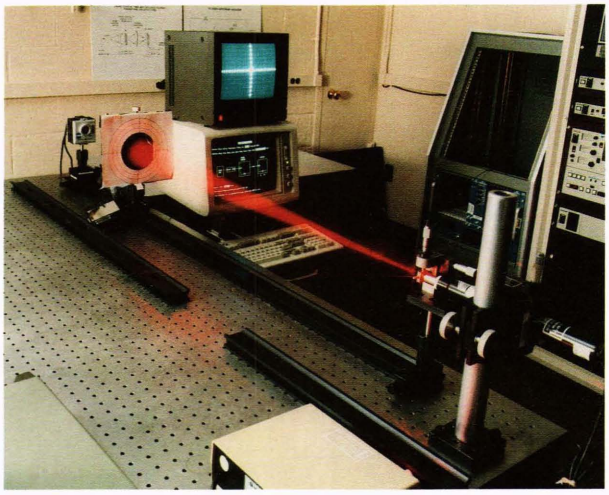

Figure 15—Photograph of the two-dimensional LCTV spectrum analyzer. Note the spectrum of the blank LCTV pixel array on the television monitor and the laser beam expansion.

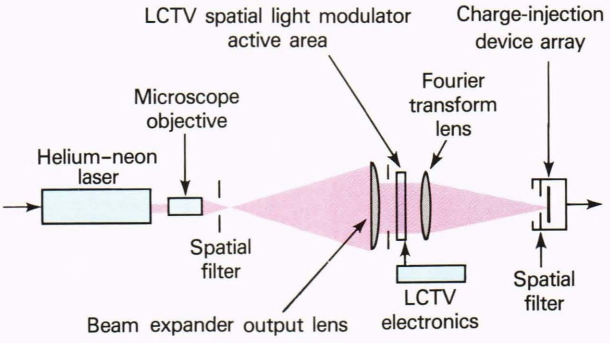

Figure 16—Two-dimensional optical-processing architecture for the video spectrum analyzer.

$$a(x,y) = [\text{rect}\,(2x/a)\ \text{rect}\,(2y/b)] * [\text{comb}\,(x/A)\ \text{comb}\,(y/B)]\ , \qquad (11)$$

where $a(x,y)$ is the rectangular aperture, rect $(2x/a)$ rect $(2y/b)$ represents the rectangular aperture of a single LCTV pixel of size $a/2$ by $b/2$ (the overall aperture also truncates the expression of Eq. 11, but this will be neglected), the asterisk represents convolution, and comb (x/A) comb (y/B) represents the pixel array sampling effect, with sample spacing A and B along the x and y axes, respectively. The result of convolution of the comb function and the rect function is a replication of the center rectangle over the entire LCTV plane, yielding the pixel pattern shown in Fig. 10 and described in the inset.

The resulting Fourier transform $A(f_x, f_y)$, only within the first (Nyquist) interval, is given by

$$A(f_x,f_y) = (AB/4)\ \text{sinc}\,(Af_x/2)\ \text{sinc}\,(Bf_y/2)\ , \qquad (12)$$

where f_x and f_y are the spatial frequencies along the x and y axes, respectively, and A and B are the sample spacings along the x and y axes, respectively. The theoretical Fourier transform and the corresponding measured Fourier transform are shown in Fig. 17. In testing the ability of the LCTV to provide a clean (high signal-to-noise ratio) input for Fourier transformation, various synthetically generated inputs were used and their transforms were generated, such as those shown in Figs. 18a to 18d. The diagonal bar pattern yields a transform with its predominant frequency content along an axis at an angle perpendicular to the diagonal bar pattern. The cosine wave pattern along both axes yields a delta function at positive and negative frequencies in the Fourier plane.

Of interest in SAR image formation is the ability of the LCTV architecture to reconstruct a rectangular ob-

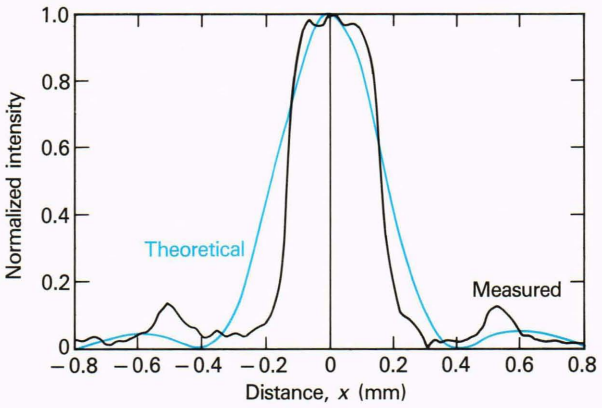

Figure 17—Theoretical and measured Fourier transforms of the LCTV pixel pattern within the first Nyquist interval.

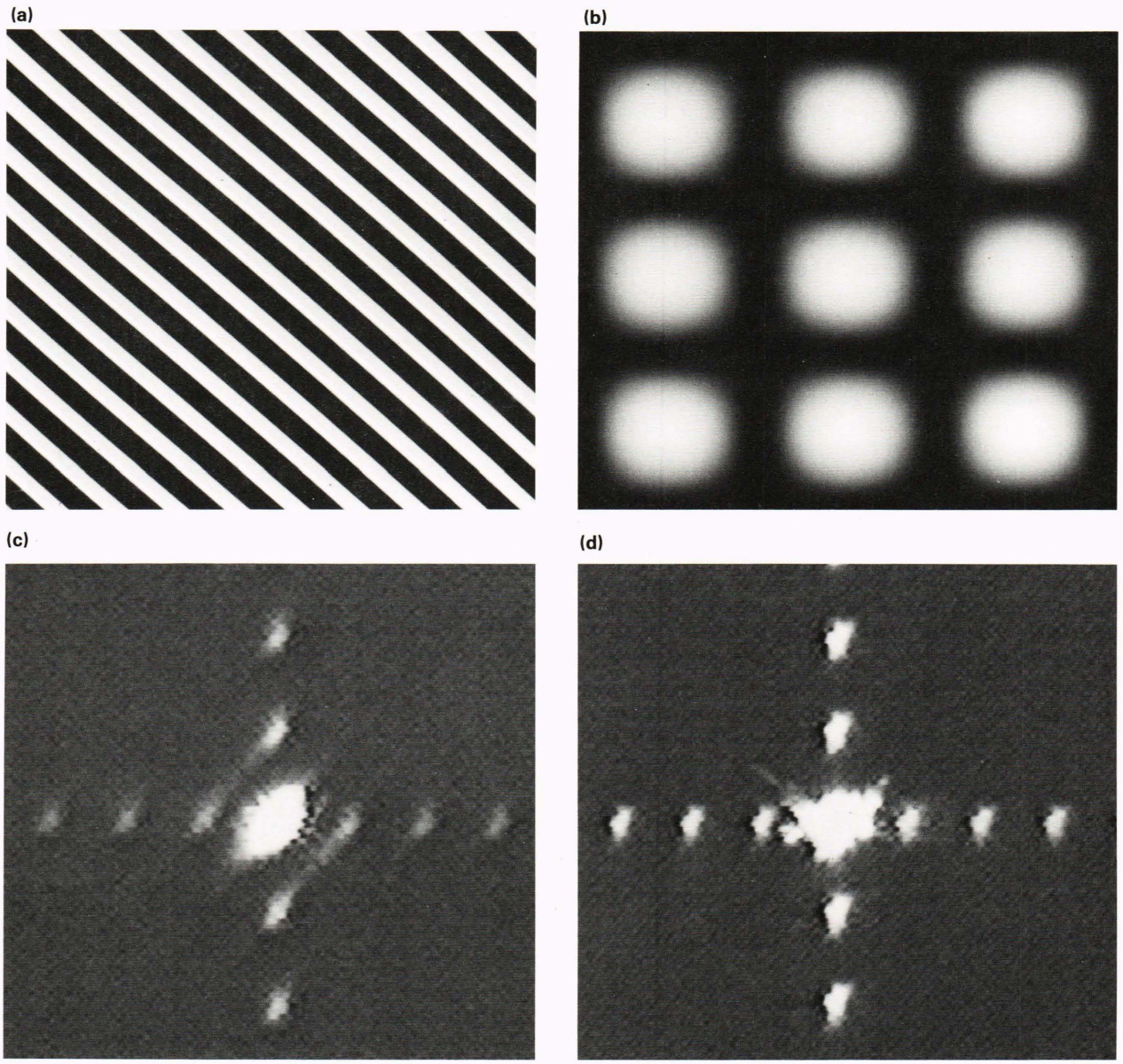

Figure 18—Synthetic LCTV input patterns: (a) diagonal square-wave bar pattern and (b) two orthogonal cosine patterns; their corresponding transforms are shown in parts c and d, respectively.

ject in the Fourier plane. Such a rectangular shape is the lowest order approximation to a realistic shape, such as the plan view of a ship. To create such an image, a sinc^2 function must be injected into the LCTV; the subsequent Fourier transform should be a rectangular shape, replicated at each side lobe position caused by the LCTV pixel array. Hence, the corruption caused by the pixel array must be removed to reconstruct the true object. This corruption is multiplicative in the LCTV plane and, by the convolution theorem, it is a convolution in the transform plane. Thus, removal of the corruption can be demonstrated by using a two-dimensional deconvolution algorithm as a postprocessing step. This result is shown in Fig. 19 for deconvolution of Fig. 18d. Deconvolution fails to recover the correct image because signal-to-noise is too low and the mainlobe is saturated.

These results show that the LCTV pixel structure has a very corrupting effect on the Fourier transform of video signals. This effect can be ameliorated to some extent by redesigning the LCTV. By making the pixel size smaller and the number of pixels greater to match the detector array, the quality of the reconstructed image can be increased and the overall size of the architecture can be decreased.

The limited dynamic range of the LCTV and its effect on the Fourier transform can be modeled by calculating the in-phase (I) or quadrature (Q) components of a low-bit-level image fast Fourier transformed on a digital computer. The results of comparing reconstructed objects with ideal patterns were derived by using a mean-square-error criterion. Mean square error between low-bit-level and 8-bit images is plotted versus bit level in Fig. 20. One example of the synthetic shapes used for reconstruction is shown in Fig. 21. From Fig. 20 we can conclude that when the image to be transformed has 4 bits of dynamic range (16 gray levels), the accuracy of the reconstructed object is asymptotically close to the 8-bit image. Hence, the dynamic range of the LCTV is actually sufficient for modest-quality SAR image generation.

The fact that only in-phase or quadrature components are required for reconstruction[18] means that two channels of data input to the LCTV may not be required, although raster video (interlaced) modulation is easily compatible with two-channel (complex) processing. The use of RF demodulators running at intermediate frequencies of 60 MHz makes the prospect of interfacing LCTV spatial light modulators to typical radar intermediate-frequency subsystems (at 60 MHz) easy to accept. From these considerations, we have greater confidence that a modest-resolution (256-by-256-pixel) SAR image-formation processor module could be implemented by using LCTV and charge-injection device technology.

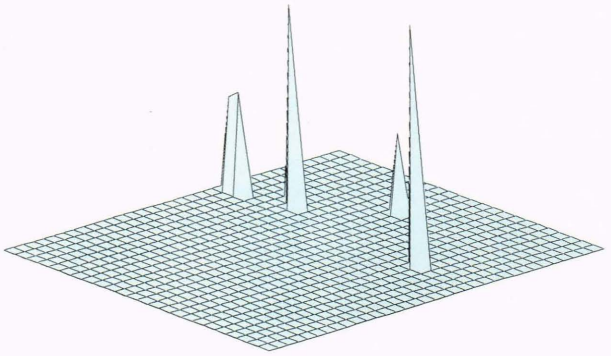

Figure 19—Deconvolved Fourier transform of an input image having two orthogonal cosine wave inputs (the original image is similar to Fig. 18d).

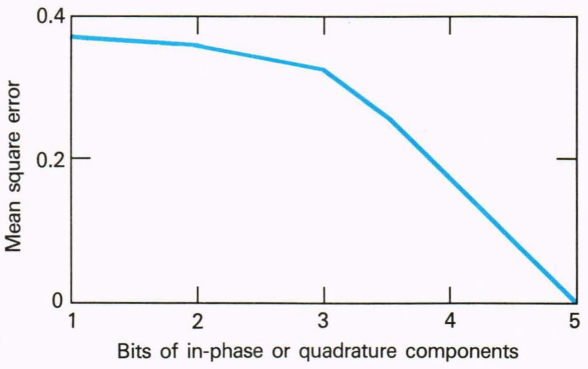

Figure 20—Mean square error between ideal images and their reconstruction via digital Fourier transformation for various bit levels.

CONCLUSIONS AND FUTURE WORK

From the measurements of laser diode coherency, calculations of power loss through the acousto-optic architecture, and considerations of multitone signal strength, we conclude that current state-of-the-art single-laser diodes do not simultaneously have the power and coherence to adequately support requirements for high-bandwidth, high-dynamic-range SAR image generation on a single-look basis. This conclusion naturally points to laser diode arrays that can be mode locked to a single high-bandwidth drive circuit. Recent developments in this area are encouraging.[17,19,20] When laser diode arrays of sufficient performance are made available and when wideband, multitone, intermediate-frequency simulators are interfaced to the Bragg cells, wideband simulations can better emulate real-world signals, and the results can be compared with those of other investigators.[14] We hope that this technology can be properly evaluated before advanced development.

Our characterization and use of LCTVs have revealed severe limitations on resolution and dynamic range. Resolution can be improved by increasing the number of pixels by about a factor of 2, and aperture size can be reduced by about a factor of 7. These changes would match LCTVs well to existing charge-coupled device (or charge-injection device) detector arrays and would reduce overall processor size. Dynamic range can be improved by upgrading the polarizer quality, but analysis shows that low dynamic range in the input plane may not be so detrimental. Certainly, low dynamic range would not preclude effective image matching, a fact that

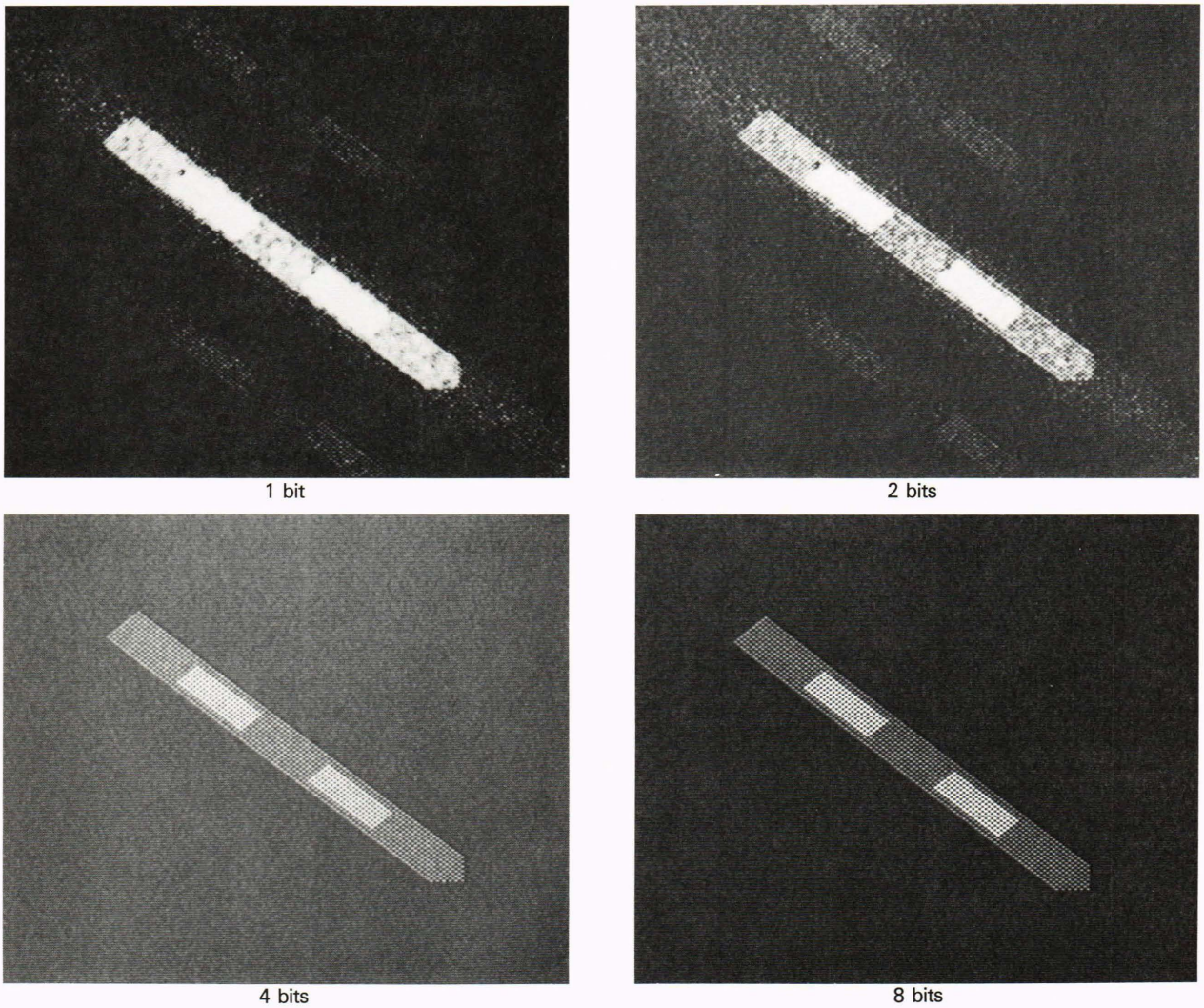

Figure 21—Examples of reconstruction for a simple ship-like object at various bit levels.

has been known for some time and one that certainly has not eluded the developers of missile guidance systems based on image correlation. It would also be desirable to speed up the frame rate of LCTVs to about 300 Hz, although this rate is not essential in some applications. In SAR image formation, a fast frame rate is not mandatory because aperture times required for just acquiring the SAR video are on the order of 1 s.

Recent conceptual design work has addressed some new ways of using LCTVs that incorporate video feedback. These techniques are geared more toward feature extraction from SAR images (or any other images, for that matter) than SAR image formation. Fourier as well as other transforms can be calculated at video rates. Correlation of SAR images for the purpose of feature extraction rather than guidance-system updating can also be accomplished by using video feedback. These concepts are the objective of future work at APL in optical processing. They promise to solve numerous postprocessing operations in a reasonably fast, inexpensive, and simple way using existing (commercial) LCTVs without always suffering the attendant degradations discussed in this article. In the long run, improvement of the properties of LCTVs or similar two-dimensional spatial light modulators is very desirable.

REFERENCES

[1] A. Sommerfeld, "Optics," in *Lectures on Theoretical Physics*, Vol. IV, Academic Press, New York (1954).
[2] E. Abbe, *Arch. Mikrosk. Anat. Entwicklungsmech.* **9**, 413 (1893).
[3] F. Zernike, "Das Phasenkontrastverfahren beider Mikroskopischen Beoachtung," *Z. Tech. Phys.* **16**, 454 (1935).
[4] J. W. Goodman, "Architectural Development of Optical Data Processing Systems," *Aust. J. Electr. Electron. Eng.* **2**, 139 (1982).
[5] L. J. Cutrona, E. N. Leith, L. J. Porcello, and W. E. Vivian, "On the Application of Coherent Optical Processing Techniques to Synthetic Aperture Radar," *Proc. IEEE* **54**, 1026 (1966).
[6] D. Casasent and D. Psaltis, "New Optical Transforms for Pattern Recognition," *Proc. IEEE* **65**, 77 (1977).
[7] A. B. Van der Lugt, "Signal Detection by Complex Spatial Filtering," *IEEE Trans. Inf. Theory* **IT-10**, 139 (1964).
[8] B. Lambert, "Wideband Instantaneous Spectrum Analyzers Employing Delay Line Light Modulators," *Int. IRE Nat. Conv. Rec.* **10**, 69 (1962).
[9] T. E. Bell, "Optical Computing: A Field in Flux," *IEEE Spectrum*, 34–57 (Aug 1986).
[10] D. Casasent, F. Caimi, and A. Khomenko, "Test and Evaluation of the Soviet Prom and Priz Spatial Light Modulators," *Appl. Opt.* **20**, 4215 (1981).

[11] D. Casasent, "Hybrid Optical/Digital Image Pattern Recognition: A Review," *SPIE Semin. Proc.* **528**, 64–82 (1985).
[12] A. E. Spezio, J. Lee, and G. W. Anderson, "Acousto-Optics for Systems Applications," *Microwave J.* **155** (Feb 1985).
[13] M. Haney and D. Psaltis, "Acoustooptic Techniques for Real-Time SAR Processing," *SPIE Semin. Proc.* **545**, 108–117 (1985).
[14] K. T. Stalker, P. A. Molley, and F. M. Dickey, *Real-Time Optical Processor for Synthetic Aperture Radar Image Formation*, Sandia National Laboratories Report SAND-87-1268C (1987).
[15] D. Psaltis, *Acousto-Optic Processing of 2-D Signals Using Temporal and Spatial Integration*, AFOSR-TR-83-1100, Appendix IIIa (31 May 1983).
[16] D. L. Hecht, "Multifrequency Acoustooptic Diffraction," *IEEE Trans. Sonics Ultrason.* **SU-24**, 7 (1977).
[17] B. Ansell, NASA Tech. Brief NPO-16198, Vol. 12, No. 6, p. 38 (Jun 1988).
[18] P. Lafrance and J. J. Ousborne, *IEEE Trans. Aerosp. Electron. Syst.* **AES-23**, 152 (1987).
[19] B. Ansell, NASA Tech. Brief NPO-16254, Vol. 12, No. 6, p. 40 (Jun 1988).
[20] Z.-L. Liau, "Surface-Emitting Semiconductor Laser for Monolithic 2D Arrays," *Inside R&D*, 2 (3 Feb 1988).

ACKOWLEDGMENTS—The contribution of Patricia Murphy to the calculation of low-bit-level fast Fourier transforms and their mean square errors and the guidance and assistance of Donald Duncan on the laser diode coherence measurements are gratefully acknowledged.

THE AUTHORS

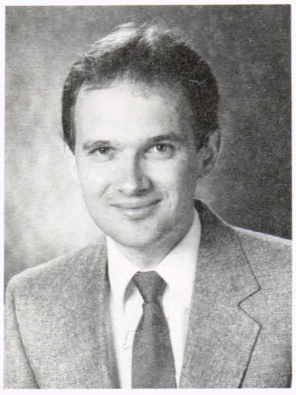

BRADLEY G. BOONE is Supervisor of the Image and Signal Processing Section of APL's Electro-Optical Systems Group. He received his Ph.D. degree from the University of Virginia in 1977. Since joining APL in 1977, he has worked on a variety of projects related to lasers, optical and infrared sensors, imaging radar, and pattern recognition. Dr. Boone has served as technical leader for the Harpoon Guidance Improvements project, which has focused on autonomous target recognition. Recently he served as technical editor of a development options paper for advanced guidance for antiship cruise missiles. He is principal investigator of several internal research and development projects covering optical signal processing, superconducting sensors and MIMIC devices, and neural networks. He is a member of the faculty of The Johns Hopkins University G.W.C. Whiting School of Engineering.

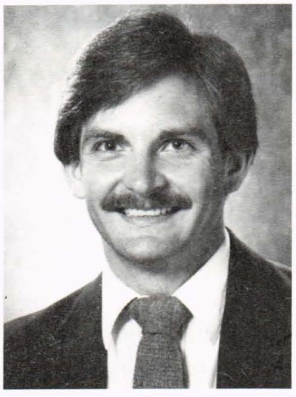

SCOTT A. GEARHART graduated from the Pennsylvania State University in 1982 with a B.S. degree in engineering science. He received an M.S. degree in electrical engineering from the University of Maryland in 1987. Mr. Gearhart joined APL in 1983 and has worked primarily on the development and evaluation of optical and infrared sensors for guidance and surveillance applications. He has also participated in IR&D efforts in optical radar processing and laser remote sensing, as well as biomedical studies in laser angiography and laser Doppler velocimetry of simulated blood flow.

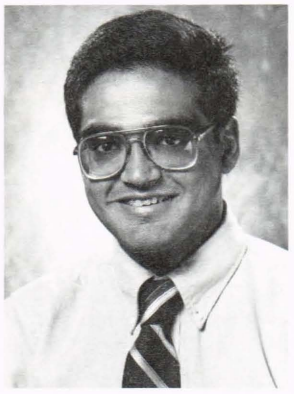

OODAYE B. SHUKLA received his B.S. in electrical engineering from Pennsylvania State University in 1986. During 1987, he worked in the Digital Flight Systems Group in APL's Space Department designing hardware. Since completing the 1987 Associate Staff Training Program, he has been a member of the Electro-Optics Group, designing and analyzing optical processing architectures.

DAVID H. TERRY graduated in 1987 from The Johns Hopkins University with B.S.E.E. and M.S.E. degrees in electrical engineering and computer science. From 1984 to 1987, he served as a research aide in the Pediatrics Department of the Johns Hopkins Medical Institutions. During the summer of 1986, he worked in the Design Assurance Department of the Fairchild Communications and Electronics Co. He joined APL's Electro-Optical Systems Group in 1987 and worked on signal processing techniques for real-time synthetic aperture radar image generation. After participation in the 1987 Associate Staff Training Program, he rejoined the Group and is working on autonomous target recognition algorithms, optical signal processing techniques, and high-temperature superconducting MIMIC circuit design.